Experimental Realization of Floquet $\mathcal{PT}$-Symmetric Systems

Mahboobeh Chitsazi, Huanan Li, F. M. Ellis, and Tsampikos Kottos

Department of Physics, Wesleyan University, Middletown, Connecticut 06459, USA

We provide an experimental framework where periodically driven $\mathcal{PT}$-symmetric systems can be investigated. The setup, consisting of two ultra high frequency oscillators coupled by a time-dependent capacitance, demonstrates a cascade of $\mathcal{PT}$-symmetric broken domains bounded by exceptional point degeneracies. These domains are analyzed and understood using an equivalent Floquet frequency lattice with local $\mathcal{PT}$ symmetry. Management of these $\mathcal{PT}$-phase transition domains is achieved through the amplitude and frequency of the drive.

Introduction.—Non-Hermitian Hamiltonians $\mathcal{H}$ which commute with the parity-time ($\mathcal{PT}$) symmetry operator might have a real spectrum when some parameter γ, controlling the degree of non-Hermiticity, is below a critical value $\gamma_{\mathcal{PT}}$ [1]. In this parameter domain, termed the *exact $\mathcal{PT}$ phase*, the eigenfunctions of $\mathcal{H}$ are also eigenfunctions of the $\mathcal{PT}$ operator. In the opposite limit, coined the *broken $\mathcal{PT}$ phase*, the spectrum consists (partially or completely) of pairs of complex conjugate eigenvalues while the eigenfunctions cease to be eigenfunctions of the $\mathcal{PT}$ operator. The transition point $\gamma = \gamma_{\mathcal{PT}}$ shows all the features of an exceptional point (EP) singularity where both eigenfunctions and eigenvalues coalesce. Its existence played a prominent role in many $\mathcal{PT}$ studies ranging from optics [2–18], matter waves [19,20] and magnonics [21,22] to acoustics [23–25] and electronics [26–28]. Subsequent experimental demonstrations [4,9,10,12–14,17,18,24–26,29] revealed the viability and technological impact of many of these studies.

Though the exploitation of $\mathcal{PT}$-symmetric systems has been prolific, most of the attention has been devoted to static (i.e., time-independent) potentials. Recently, however, a parallel activity associated with time-dependent $\mathcal{PT}$-symmetric systems has started to attract increasing attention [30–40]. The excitement for this line of research stems from two reasons: the first is fundamental and associated with the expectation that new pathways in the $\mathcal{PT}$ arena can lead to new exciting phenomena. This expectation is further supported by the fact that the investigation of time-dependent Hermitian counterparts led to a plethora of novel phenomena—examples include Rabi oscillations [41], Autler-Townes splitting [42], dynamical localization [43], dynamical Anderson localization [44], and coherent destruction of tunneling [45,46] (for a review see Ref. [47]). The second reason is technological and it is associated with the possibility to use driving schemes as a flexible experimental knob to realize new forms of *reconfigurable* synthetic matter [48,49]. Specifically, in the case of $\mathcal{PT}$-symmetric systems one hopes that the use of periodic driving schemes can allow for

management of the spontaneous $\mathcal{PT}$-symmetry breaking for *arbitrary values of the gain and loss parameter*. The basic idea behind this is that periodic driving can lead to a renormalization of the coupling and a consequent tailoring of the position of the EPs. Unfortunately, while there is a number of theoretical studies [31,34,36,39] advocating for this scenario, there is no experimental realization of a time-dependent $\mathcal{PT}$-symmetric setup (See *Note added.*).

Here we provide such an experimental platform where periodically driven $\mathcal{PT}$-symmetric systems can be investigated. Our setup [see Figs. 1(a) and 1(b)] consists of two coupled LC resonators with balanced gain and loss. The capacitance that couples the two resonators is parametrically driven with a network of varactor diodes. We find that this driven $\mathcal{PT}$ system supports a sequence of spontaneous $\mathcal{PT}$-symmetry broken domains bounded by exceptional point degeneracies. The latter are analyzed and understood theoretically using an equivalent Floquet frequency lattice with local $\mathcal{PT}$ symmetry. The position and size of these instability islands can be controlled through the amplitude and frequency of the driving and can be achieved, in principle, for arbitrary values of the gain or loss parameter.

Experimental setup.—A natural frequency of $\omega_0/2\pi = 235$ MHz was chosen as the highest frequency convenient for a simple implementation of electronic gain and loss. The $L = 32$ nH inductors of Fig. 1(a) are two-turns of
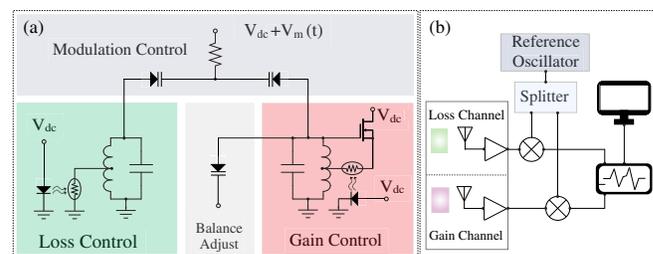

FIG. 1. (a) Experimental $\mathcal{PT}$ circuit with tuning and modulation control. (b) Signal control and analysis system.
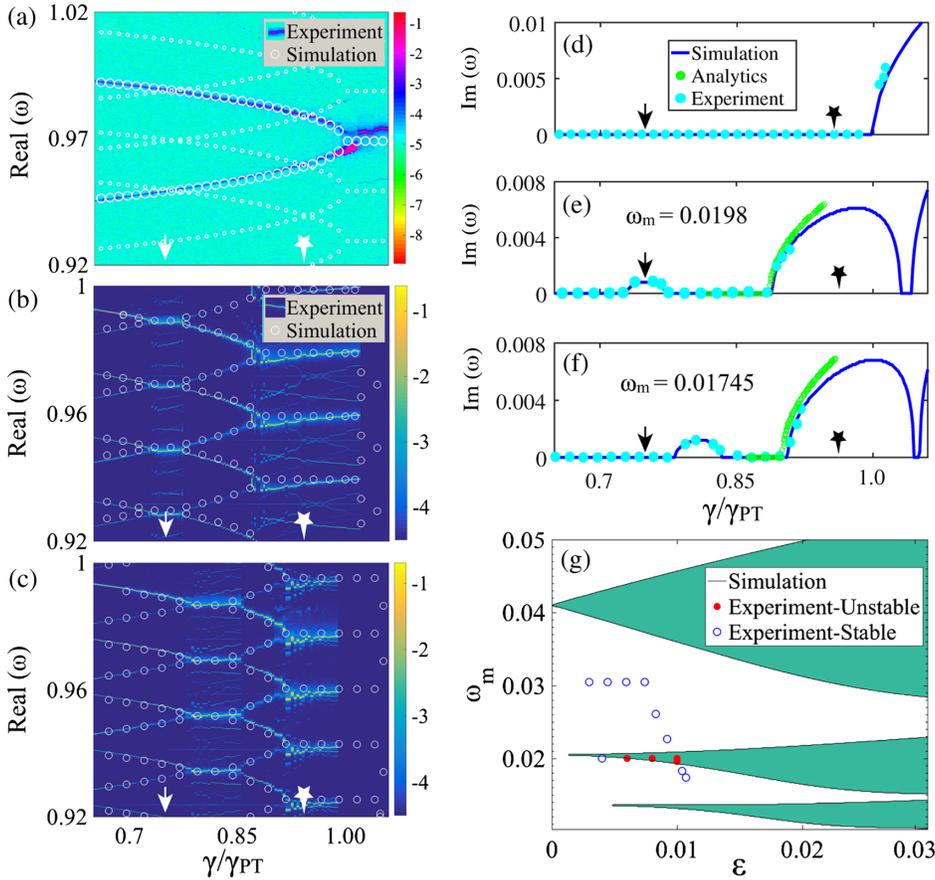
FIG. 2. Spectral density plots for $Re(\omega)$ of the RLC dimer of Fig. 1, with $c_0 = 0.0671$ and $\epsilon = 0.01$. (a) Undriven dimer $\epsilon = 0$. The white circles show the expected ladder $\omega_{1,2} + n\omega_m$ associated with the eigenfrequencies of $H_{F,0}$ for $\omega_m = 0.0198$. (b) The crossing points "evolve" to flat regions when the system is driven. (c) For a different driving frequency $\omega_m = 0.01745$ the flat regions shift to different γ domains. The white circles in (b) and (c) represent the results of the simulations and match the dominant bands of the density plots within the corresponding $\log_{10}$ color schemes. The domain shift with drive frequency is more clearly seen in $\mathcal{I}m(\omega)$ from experiment (aqua circles), numerics (blue line), and perturbation theory Eq. (10) (green circles) for: (d) an undriven and (e),(f) driven dimers, with ω_m shown. The arrows and stars indicate the fixed crossing point in (a) for reference. Finally, (g) shows an (ϵ, ω_m) map of the $\mathcal{PT}$-exact (white) and -broken (shaded) phases for $\gamma/\gamma_{\mathcal{PT}}$ fixed at the position of the arrows.

1.5 mm diameter Cu wire with their hot ends supported by their corresponding parallel $C = 15$ pF on opposite sides of a grounded partition separating gain and loss compartments. Gain and loss (corresponding to effective parallel resistances $\mp R$) are directly implemented via Perkin-Elmer V90N3 photocells connecting the center turn of each inductor either directly to ground (loss side) or to a BF998 MOSFET following the LC node (gain side). Thus as both photocells experience the same voltage drop, the loss side photocell extracts its current from the tap point while the gain side photocell injects its current into the tap point. The photocells are coupled to computer driven LEDs through 1 cm light pipes for RF isolation. As the gain of the MOSFET is changed, its capacitance shifts slightly, unbalancing the resonators. A BB135 varactor is used to compensate for these changes.

The capacitance coupling network, implemented by similar varactors, is optimized for application of a modulation frequency in the vicinity of 4.6 MHz while simultaneously providing the dc bias necessary for controlling the inter-resonator coupling C_c.

Figure 1(b) shows the remainder of the signal acquisition setup. The excitation in each resonator is sensed by a small pickup loop attached to the input of a Minicircuits ZPL-1000 low noise amplifier. The gain and loss pick-up channels are then hetrodyned to ≈ 30 MHz before being captured by a Tektronix DPO2014 oscilloscope.

The experimental unmodulated $\mathcal{PT}$ diagram, shown with the color map in Fig. 2(a), is matched to the theoretical results in order to calibrate both the resonator frequency balance and the gain or loss balance. The coupling is then modulated, directly comparing each calibrated point with and without the modulation. Signal transients are measured by pulsing the MOSFET drain voltage at approximately 1 kHz and capturing the resonator responses on both the gain and loss sides. The captured signals can be frequency analyzed to obtain the modulated (or unmodulated) spectrum, see Fig. 2. Close attention has to be paid to avoid saturation of any of the components in the signal pick-up chain.

Theoretical considerations.—Using Kirchoff's laws, the dynamics for the voltages $V_1(V_2)$ of the gain (loss) side of the periodically driven dimer is

$$\frac{d^2}{d\tau^2}V + A\frac{d}{d\tau}V + BV = 0; \quad V \equiv (V_1, V_2)^T, \qquad (1)$$

where $\tau = \omega_0 t$ is the rescaled time, $\omega_0 = 1/\sqrt{LC}$ and

$$A = \frac{1}{\beta}\begin{bmatrix} -\gamma(1+c) + 2\dot{c} & \gamma c - 2\dot{c} \\ -\gamma c - 2\dot{c} & \gamma(1+c) + 2\dot{c} \end{bmatrix},$$

$$B = \frac{1}{\beta}\begin{bmatrix} 1 + c + \ddot{c} & c - \ddot{c} \\ c - \ddot{c} & 1 + c + \ddot{c} \end{bmatrix}. \qquad (2)$$

Above $\beta = 1 + 2c$, $\gamma = R^{-1}\sqrt{L/C}$ is the rescaled gain or loss parameter, and $\dot{c}$ ($\ddot{c}$) denotes the first (second) derivative of the scaled capacitive coupling $c \equiv C_c/C = c_0 + \epsilon \cos(\omega_m \tau)$ with respect to the scaled time τ. Equation (1) is invariant under joint parity $\mathcal{P}$ and time $\mathcal{T}$ operations, where $\mathcal{T}$ performs the operation $\tau \to -\tau$ and $\mathcal{P}$ is the Pauli matrix σ_x.

The eigenfrequencies $\omega_\alpha (\alpha = 1, 2)$ of system Eq. (1) in the absence of driving are given as

$$\omega_\alpha = \frac{1}{2\sqrt{1 + 2c_0}}\left(\sqrt{\gamma_c^2 - \gamma^2} + (-1)^\alpha\sqrt{\gamma_{PT}^2 - \gamma^2}\right) \quad (3)$$

where the spontaneous $\mathcal{PT}$-symmetry breaking point and the upper critical point can be identified as $\gamma_{PT} = \sqrt{1 + 2c_0} - 1$ and $\gamma_c = \sqrt{1 + 2c_0} + 1$, respectively, and they are both determined by the strength of the (capacitance) coupling between the two elements of the dimer. A parametric evolution of these modes, versus the gain or loss parameter γ, is shown in Fig. 2(a) where the open circles represent Eq. (3) and the color map shows the experimental results. We find that the spectrum of the undriven dimmer is divided in two domains of exact ($\gamma < \gamma_{PT}$) and broken ($\gamma > \gamma_{PT}$) $\mathcal{PT}$-symmetry phase.

In order to investigate the effects of driving we now turn to the Floquet picture. We therefore employ a Liouvillian formulation of Eq. (1). The latter becomes

$$\frac{d\psi}{d\tau} = \mathcal{L}\psi, \qquad \mathcal{L} = \begin{bmatrix} 0 & I_2 \\ -B & -A \end{bmatrix}, \qquad \psi = \begin{pmatrix} V \\ \dot{V} \end{pmatrix} \quad (4)$$

and allows us to make equivalences with the time-dependent Schrödinger equation by identifying a non-Hermitian effective Hamiltonian $H_{\text{eff}} = \iota\mathcal{L}$.

The general form of the solution of Eq. (4) is given by Floquet's theorem which in matrix notation reads $F(\tau) = \Phi(\tau)e^{-\iota Q\tau}$ with $\Phi[\tau + (2\pi/\omega_m)] = \Phi(\tau)$, Q a Jordan matrix, and $F(\tau)$ a 4×4 matrix consisting of four independent solutions of Eq. (4). The eigenvalues of Q are the characteristic exponents (quasienergies) which determine the stability properties of the system: namely, the system is stable (exact $\mathcal{PT}$ phase) if all the quasienergies are real and it is unstable (broken $\mathcal{PT}$ phase) otherwise. We can evaluate the quasienergies by constructing the evolution operator $U(\tau, 0) = F(\tau)F^{-1}(0)$ via numerical integration of Eq. (5) [or of Eq. (1)]. Then the quasienergies are the eigenvalues of $1/(-\iota 2\pi/\omega_m) \ln U(\tau = 2\pi/\omega_m, 0)$.

In Figs. 2(a)–2(g) we report our numerical findings together with the experimentally measured values of the quasienergies versus the gain or loss parameter. Figures 2(a) and 2(d) show the unmodulated situation. Figures 2(b) and 2(e) show the behavior at modulation frequency $\omega_m = 0.0198$ and modulation amplitude $\epsilon = 0.01$. Finally, Figs. 2(c) and 2(f) show the evolution of the spectrum with a small change in modulation frequency ω_m for fixed ϵ. See the Supplemental Material [50] for details of the analysis.

We find several new features in the spectrum of the driven $\mathcal{PT}$-symmetric systems. The first one is the existence of a cascade of domains for which the system is in the broken $\mathcal{PT}$ phase. These domains are identified by the flat regions, seen in Figs. 2(b) and 2(c) where the real parts of eigenfrequencies have merged in the vicinity of the crossing points (indicated by the arrows and stars) and the emerging nonzero imaginary parts shown in Figs. 2(d)–2(f). The size and position of these unstable "bubbles" are directly controlled by the values of the driving amplitude ϵ, compare Figs. 2(a) and 2(d) with Figs. 2(b) and 2(e) or by the driving frequency ω_m, compare Figs. 2(b) and 2(e) with Figs. 2(c) and 2(f). The bubbles are separated by γ domains where the system is in the exact (stable) $\mathcal{PT}$ phase. The transition between stable and unstable domains occurs via a typical EP degeneracy [notice the square-root singularities in Figs. 2(d)–2(f)]. Eventually, the system becomes unstable beyond some critical gain or loss value $\gamma_{\max}$ which is defined as the maximum value of the gain or loss parameter above which there are no further stability domains. Generally $\gamma_{\max}$ depends on both ϵ and ω_m and in the limit of $\epsilon = 0$ becomes equal to γ_{PT}. Figure 2(g) maps the numerically determined $\mathcal{PT}$ exact (white) and broken (shaded) phases for γ fixed at the position of the arrows in the accompanying plots.

A theoretical understanding of the spectral metamorphosis from a single exact or broken phase to multiple domains of broken and preserved $\mathcal{PT}$ symmetry, as ϵ increases from zero, is achieved by utilizing the notion of Floquet Hamiltonian H_F. To this end, we first introduce a time-dependent similarity transformation $\mathcal{R}$ (see Supplemental Material [50]), which brings H_{eff} to a symmetric form. Under this transformation, Eq. (4) takes the form

$$\iota\frac{d}{d\tau}\tilde{\psi} = \tilde{H}\tilde{\psi}; \quad \tilde{H} \equiv \mathcal{R}H_{\text{eff}}\mathcal{R}^{-1} - \iota\mathcal{R}\frac{d}{d\tau}\mathcal{R}^{-1} \quad (5)$$

which dictates the evolution of the transformed state $\tilde{\psi} = \mathcal{R}\psi$. The matrix $\tilde{H}$ has the form

$$\tilde{H} = \tilde{H}^T = \begin{bmatrix} -\frac{3}{2}\frac{\iota\dot{c}}{\beta} & c_+ + \frac{\iota\gamma}{2\sqrt{\beta}} & c_- + \frac{\iota\gamma}{2\sqrt{\beta}} & \frac{3}{2}\frac{\iota\dot{c}}{\beta} \\ c_+ + \frac{\iota\gamma}{2\sqrt{\beta}} & \frac{\iota c^{(3)}}{2(1+2\ddot{c})} & -\frac{\iota c^{(3)}}{2(1+2\ddot{c})} & c_- - \frac{\iota\gamma}{2\sqrt{\beta}} \\ c_- + \frac{\iota\gamma}{2\sqrt{\beta}} & -\frac{\iota c^{(3)}}{2(1+2\ddot{c})} & \frac{\iota c^{(3)}}{2(1+2\ddot{c})} & c_+ - \frac{\iota\gamma}{2\sqrt{\beta}} \\ \frac{3}{2}\frac{\iota\dot{c}}{\beta} & c_- - \frac{\iota\gamma}{2\sqrt{\beta}} & c_+ - \frac{\iota\gamma}{2\sqrt{\beta}} & -\frac{3}{2}\frac{\iota\dot{c}}{\beta} \end{bmatrix}, \quad (6)$$

where $c_\pm = \frac{1}{2} \pm \frac{1}{2}(\sqrt{1 + 2\ddot{c}}/\sqrt{\beta})$ and $c^{(3)}$ denotes the third derivative of the capacitive coupling with respect to the scaled time τ. We can easily show that $\tilde{\mathcal{P}}\mathcal{T}\tilde{H}\tilde{\mathcal{P}}\mathcal{T} = \tilde{H}$ where $\tilde{\mathcal{P}} = \begin{bmatrix} 0 & \sigma_x \\ \sigma_x & 0 \end{bmatrix}$ and $\mathcal{T}: \tau \to -\tau, \iota \to -\iota$.

We are now ready to utilize the notion of Floquet Hamiltonian H_F whose components are given by

$$\langle \alpha, n|H_F|\beta, l\rangle = \tilde{H}^{(n-l)}_{\alpha\beta} + n\omega_m\delta_{\alpha\beta}\delta_{nl}, \qquad (7)$$

where the subscripts $\alpha, \beta = 1, 2, 3, 4$ label the components of $\tilde{H}$, see Eq. (6), n, l are any integers, and $\tilde{H}^{(n)}_{\alpha\beta} = 1/(2\pi/\omega_m)\int_0^{2\pi/\omega_m}\tilde{H}_{\alpha\beta}(\tau)e^{-\imath n\omega_m\tau}d\tau$. In this picture the quasienergies are the eigenvalues of the Floquet Hamiltonian H_F. Equation (7) defines a lattice model [51] with connectivity given by the off-diagonal elements of H_F and an on-site gradient potential $n\omega_m$.

Within the first order approximation to the strength of the driving amplitude ε and the modulation frequency $\omega_m \sim \mathcal{O}(\epsilon)$, the Floquet Hamiltonian is symmetric and takes the block-tridiagonal form $H_F = H_{F,0} + \varepsilon H_{F,1} + O(\varepsilon^2)$ where $\langle n|H_{F,0}|n\rangle = \tilde{H}^{(0)}|_{\varepsilon=0} + n\omega_m I_4$ consists of the diagonal blocks of H_F while $\langle n+1|H_{F,1}|n\rangle = \langle n|H_{F,1}|n+1\rangle = X$ consist of off-diagonal blocks of H_F. The 4×4 matrix X has the form

$$X = \frac{\imath}{4(1+2c_0)^{3/2}}\begin{bmatrix} 0 & \imath-\gamma & -\imath-\gamma & 0 \\ \imath-\gamma & 0 & 0 & -\imath+\gamma \\ -\imath-\gamma & 0 & 0 & \imath+\gamma \\ 0 & -\imath+\gamma & \imath+\gamma & 0 \end{bmatrix}. \qquad (8)$$

Next we proceed with the analytical evaluation of the quasienergies. First, we neglect the off-diagonal block matrices $H_{F,1}$ and diagonalize $H_{F,0}$. To this end, we construct a similarity transformation $P_0^{-1}\tilde{H}^{(0)}|_{\varepsilon=0}P_0 = \text{diag}\{\omega_2, \omega_1, -\omega_1, -\omega_2\}$. Correspondingly the eigenvalues of $H_{F,0}$ are simply $\{\omega_2 + n\omega_m, \omega_1 + n\omega_m, -\omega_1 + n\omega_m, -\omega_2 + n\omega_m\}$; i.e., the spectrum resembles a ladder of step ω_m with the basic unit associated with the eigenfrequencies of the undriven dimer Eq. (3). The resulting ladder spectrum (white circles) is shown in Fig. 2(a) versus the gain or loss parameter γ. Level crossing occurs at some specific values of $\gamma^{(j)} < \gamma_{\mathcal{PT}}$, i.e., $\omega_2|_{\gamma^{(j)}} = \omega_1|_{\gamma^{(j)}} + j\omega_m$. When the driving amplitude ε is turned on, the crossing points evolve to broken $\mathcal{PT}$-symmetry domains with respect to gain or loss parameter γ. The centers of the instability bubbles are associated with $\gamma^{(j)}$ which is controlled by ω_m [see Figs. 2(b) and 2(c)]. Furthermore, the real part of the eigenfrequencies become degenerate for a range of γ values around $\gamma^{(j)}$, Fig. 2(b), while an instability bubble emerges for the imaginary part—see Fig. 2(e) for numerical (blue solid lines) and experimental data (filled aqua circles). The transition points from stable to unstable domains have all the characteristic features of an EP.

To understand this phenomenon, we consider the effect of the off-diagonal term $\varepsilon H_{F,1}$. For simplicity, we focus on the unstable region around the crossing point at $\gamma^{(1)}$. Application of degenerate perturbation theory to the nearly degenerate levels ω_2 and $\omega_1 + \omega_m$ gives

$$\omega = \frac{(\omega_2 + \omega_1 + \omega_m) \pm \sqrt{(\omega_2 - \omega_1 - \omega_m)^2 + 4\varepsilon^2\tilde{X}_{12}\tilde{X}_{21}}}{2}, \qquad (9)$$

where $\tilde{X} = P_0^{-1}XP_0$ and the subscripts indicate the corresponding matrix components. Around the EP, ω can be written as

$$\text{Re}(\omega) \approx \omega_2|_{\gamma^{(1)}}; \quad \text{Im}(\omega) = \pm C_m\sqrt{\gamma-\gamma_0}, \quad \gamma > \gamma_0 \quad (10)$$

which has the characteristic square-root singularity of EP degeneracies. The constant C_m depends on ϵ, ω_m (see Supplemental Material [50]), and γ_0 is the solution of the equation $(\omega_2 - \omega_1 - \omega_m)^2 + 4\varepsilon^2\tilde{X}_{12}(\gamma)\tilde{X}_{21}(\gamma) = 0$ [see Eqs. (8) and (9)]. For our experiment, where $\gamma_0 \to \gamma_{\mathcal{PT}}$ and $\gamma_{\mathcal{PT}} \to 0$, we estimate that

$$\gamma_0 \approx \gamma_{\mathcal{PT}}\left[1 - \left(\frac{\sqrt{2}\omega_m + \sqrt{2\omega_m^2 + \varepsilon(4\gamma_{PT} + \varepsilon)}}{4\gamma_{PT} + \varepsilon}\right)^2\right]. \qquad (11)$$

From Eq. (10) we see that both ω_m, ϵ are responsible for a renormalization of the coupling between the two levels [compare with Eq. (3)]. Predictions [Eq. (10)] are in agreement with the numerical and experimental data [see green line in Figs. 2(e) and 2(f)]. Higher orders of EPs $\gamma^{(j)}$ can be analyzed in a similar manner after incorporating higher order perturbation theory corrections. In Fig. 2(g) we report a summary of $\mathcal{PT}$ exact and broken domains in the parametric (ϵ, ω_m) space [52,53] where $\gamma/\gamma_{\mathcal{PT}} = 0.74$ [indicated by white arrow in Figs. 2(a)–2(c)]. Obvious consequences of the (ϵ, ω_m) control of stable-unstable domains can be also observed in the dynamics (see Supplemental Material [50]).

From Eq. (11) we can also deduce that for constant ω_m (determining the center of the bubble), the edges of the instability domain are pushed away when ϵ increases. Thus the broken $\mathcal{PT}$-symmetric regimes can broaden beyond the $\gamma_{\mathcal{PT}}$ border by controlling ω_m or/and ϵ. For example, in Figs. 2(e) and 2(f) we can see the revival of the exact $\mathcal{PT}$ phase around $\gamma/\gamma_{PT} = 1.07$ as the driving frequency increases. In this case, the center of the nearby instability bubble, which is controlled by ω_m, shifts to smaller γ values and eventually disappears together with the whole bubble. At the same time $\gamma_{\max}$ remains roughly unaffected. In fact in the high frequency limit, one can average out the time dependence and recover a "static" $\mathcal{PT}$-symmetric dimmer with renormalized coupling constants [39,40]. In this limit, and for small ϵ, one can easily show using Eq. (4), that $\gamma_{\max} \approx \gamma_{\mathcal{PT}}$. Consequently, the stability domain between the upper border of the $\gamma^{(1)}$ bubble and $\gamma_{\max}$ increases.

Conclusions.—We have experimentally demonstrated that $\mathcal{PT}$-symmetric systems containing periodically driven components are capable of controlling the presence, strengths, and positions of multiple exact-phase domains, bounded by corresponding exceptional points. The generic

behavior is well described by a perturbative analysis of the Floquet Hamiltonian, and opens up new directions of exceptional point management in a variety of electronic, mechanical, or optomechanical applications.

Note added.—Recently, we became aware of Ref. [54]. This contribution presents a quantum realization of a dissipative Floquet system of ultracold atoms, and the setup does not involve gain.

---

[1] C. M. Bender and S. Boettcher, Phys. Rev. Lett. **80**, 5243 (1998); C. M. Bender, Rep. Prog. Phys. **70**, 947 (2007).

[2] K. G. Makris, R. El-Ganainy, D. N. Christodoulides, and Z. H. Musslimani, Phys. Rev. Lett. **100**, 103904 (2008).

[3] S. Longhi, Phys. Rev. Lett. **103**, 123601 (2009); S. Longhi, Phys. Rev. Lett. **105**, 013903 (2010).

[4] C. E. Rüter, K. G. Makris, R. El-Ganainy, D. N. Christodoulides, M. Segev, and D. Kip, Nat. Phys. **6**, 192 (2010); A. Guo, G. J. Salamo, D. Duchesne, R. Morandotti, M. Volatier-Ravat, V. Aimez, G. A. Siviloglou, and D. N. Christodoulides, Phys. Rev. Lett. **103**, 093902 (2009).

[5] M. C. Zheng, D. N. Christodoulides, R. Fleischmann, and T. Kottos, Phys. Rev. A **82**, 010103 (2010).

[6] H. Schomerus, Phys. Rev. Lett. **104**, 233601 (2010).

[7] A. A. Sukhorukov, Z. Xu, and Y. S. Kivshar, Phys. Rev. A **82**, 043818 (2010).

[8] S. Longhi, Phys. Rev. A **82**, 031801 (2010); Y. D. Chong, L. Ge, and A. Douglas Stone, Phys. Rev. Lett. **106**, 093902 (2011).

[9] L. Feng, M. Ayache, J. Huang, Y.-L. Xu, M.-H. Lu, Y.-F. Chen, Y. Fainman, and A. Scherer, Science **333**, 729 (2011).

[10] A. Regensburger, C. Bersch, M. A. Miri, G. Onishchukov, D. N. Christodoulides, and U. Peschel, Nature (London) **488**, 167 (2012).

[11] H. Ramezani, D. N. Christodoulides, V. Kovanis, I. Vitebskiy, and T. Kottos, Phys. Rev. Lett. **109**, 033902 (2012); H. Ramezani, T. Kottos, V. Kovanis, and D. N. Christodoulides, Phys. Rev. A **85**, 013818 (2012).

[12] L. Chang, X. Jiang, S. Hua, C. Yang, J. Wen, L. Jiang, G. Li, G. Wang, and M. Xiao, Nat. Photonics **8**, 524 (2014).

[13] B. Peng, Ş. K. Özdemir, F. Lei, F. Monifi, M. Gianfreda, G. L. Long, S. Fan, F. Nori, C. M. Bender, and L. Yang, Nat. Phys. **10**, 394 (2014).

[14] H. Hodaei, M.-A. Miri, M. Heinrich, D. N. Christodoulides, and M. Khajavikhan, Science **346**, 975 (2014); L. Feng, Z. J. Wong, R.-M. Ma, Y. Wang, and X. Zhang, Science **346**, 972 (2014).

[15] N. Lazarides and G. P. Tsironis, Phys. Rev. Lett. **110**, 053901 (2013); D. Wang and A. B. Aceves, Phys. Rev. A **88**, 043831 (2013).

[16] H. Ramezani, Z. Lin, S. Kalish, T. Kottos, V. Kovanis, and I. Vitebskiy, Opt. Express **20**, 26200 (2012).

[17] Z.-P. Liu, J. Zhang, S. K. Özdemir, B. Peng, H. Jing, X.-Y. Lü, C.-W. Li, L. Yang, F. Nori, and Y.-X. Liu, Phys. Rev. Lett. **117**, 110802 (2016).

[18] B. Peng, S. K. Ozdemir, S. Rotter, H. Yilmaz, M. Liertzer, F. Monifi, C. M. Bender, F. Nori, and L. Yang, Science **346**, 328 (2014).

[19] H. Cartarius and G. Wunner, Phys. Rev. A **86**, 013612 (2012); M. Kreibich, J. Main, H. Cartarius, and G. Wunner, Phys. Rev. A **87**, 051601(R) (2013); **90**, 033630 (2014); W. D. Heiss, H. Cartarius, and G. Wunner, J. Phys. A **46**, 275307 (2013).

[20] E.-M. Graefe, J. Phys. A **45**, 444015 (2012); M. Hiller, T. Kottos, and A. Ossipov, Phys. Rev. A **73**, 063625 (2006).

[21] J. M. Lee, T. Kottos, and B. Shapiro, Phys. Rev. B **91**, 094416 (2015).

[22] A. Galda and V. M. Vinokur, Phys. Rev. B **94**, 020408(R) (2016).

[23] X. Zhu, H. Ramezani, C. Shi, J. Zhu, and X. Zhang, Phys. Rev. X **4**, 031042 (2014).

[24] R. Fleury, D. Sounas, and A. Alu, Nat. Commun. **6**, 5905 (2015).

[25] C. Shi, M. Dubois, Y. Chen, L. Cheng, H. Ramezani, Y. Wang, and X. Zhang, Nat. Commun. **7**, 11110 (2016).

[26] J. Schindler, Z. Lin, J. M. Lee, H. Ramezani, F. M. Ellis, and T. Kottos, J. Phys. A **45**, 444029 (2012); H. Ramezani, J. Schindler, F. M. Ellis, U. Günther, and T. Kottos, Phys. Rev. A **85**, 062122 (2012); Z. Lin, J. Schindler, F. M. Ellis, and T. Kottos, Phys. Rev. A **85**, 050101(R) (2012); N. Bender, S. Factor, J. D. Bodyfelt, H. Ramezani, D. N. Christodoulides, F. M. Ellis, and T. Kottos, Phys. Rev. Lett. **110**, 234101 (2013).

[27] J. Cuevas, P. G. Kevrekidis, A. Saxena, and A. Khare, Phys. Rev. A **88**, 032108 (2013); F. Bagarello, Phys. Rev. A **88**, 032120 (2013).

[28] I. V. Barashenkov and M. Gianfreda, J. Phys. A **47**, 282001 (2014).

[29] S. Assawaworrarit, X. Yu, and S. Fan, Nature (London) **546**, 387 (2017).

[30] C. T. West, T. Kottos, and T. Prosen, Phys. Rev. Lett. **104**, 054102 (2010).

[31] N. Moiseyev, Phys. Rev. A **83**, 052125 (2011).

[32] R. El-Ganainy, K. G. Makris, and D. N. Christodoulides, Phys. Rev. A **86**, 033813 (2012).

[33] G. Della Valle and S. Longhi, Phys. Rev. A **87**, 022119 (2013).

[34] X. Luo, J. Huang, H. Zhong, X. Qin, Q. Xie, Y. S. Kivshar, and C. Lee, Phys. Rev. Lett. **110**, 243902 (2013); X.-B. Luo, R.-X. Liu, M.-H. Liu, X.-G. Yu, D.-L. Wu, and Q.-L. Hu, Chin. Phys. Lett. **31**, 024202 (2014).

[35] X. Lian, H. Zhong, Q. Xie, X. Zhou, Y. Wu, and W. Liao, Eur. Phys. J. D **68**, 189 (2014).

[36] D. Psiachos, N. Lazarides, and G. P. Tsironis, Appl. Phys. A **117**, 663 (2014); G. P. Tsironis and N. Lazarides, Appl. Phys. A **115**, 449 (2014).

[37] V. V. Konotop and D. A. Zezyulin, Opt. Lett. **39**, 1223 (2014).

[38] J. D'Ambroise, B. A. Malomed, and P. G. Kevrekidis, Chaos **24**, 023136 (2014).

[39] Y. N. Joglekar, R. Marathe, P. Durganandini, and R. Pathak, Phys. Rev. A **90**, 040101(R) (2014); T. E. Lee and Y. N. Joglekar, Phys. Rev. A **92**, 042103 (2015).

[40] Y. Wu, B. Zhu, S.-F. Hu, Z. Zhou, and H. Zhong, Front. Phys. **12**, 121102 (2017).

[41] M. O. Scully and M. S. Zubairy, *Quantum Optics* (Cambridge University Press, Cambridge, England, 1997).

[42] S. H. Autler and C. H. Townes, Phys. Rev. **100**, 703 (1955).

[43] D. H. Dunlap and V. M. Kenkre, Phys. Rev. B **34**, 3625 (1986).

[44] B. V. Chirikov, F. M. Izrailev, and D. L. Shepelyansky, Sov. Sci. Rev. C **2**, 209 (1981).

[45] F. Grossmann, T. Dittrich, P. Jung, and P. Hänggi, Phys. Rev. Lett. **67**, 516 (1991).

[46] G. Della Valle, M. Ornigotti, E. Cianci, V. Foglietti, P. Laporta, and S. Longhi, Phys. Rev. Lett. **98**, 263601 (2007).

[47] M. Grifoni and P. Hänggi, Phys. Rep. **304**, 229 (1998).

[48] N. H. Lindner, G. Rafael, and V. Galitski, Nat. Phys. **7**, 490 (2011).

[49] Y. H. Wang, H. Steinberg, P. Jarillo-Herrero, and N. Gedik, Science **342**, 453 (2013).

[50] See Supplemental Material at http://link.aps.org/supplemental/10.1103/PhysRevLett.119.093901 for both the experimental and theoretical details.

[51] N. Bender, H. Li, F. M. Ellis, and T. Kottos, Phys. Rev. A **92**, 041803(R) (2015).

[52] Hartono and A. van der Burgh, J. Eng. Math. **49**, 99 (2004).

[53] F. Dohnal, J. Sound Vib. **306**, 136 (2007).

[54] J. Li, A. K. Harter, J. Liu, L. de Melo, Y. N. Joglekar, and L. Kuo, arXiv:1608.05061.